Ultramicroscopy 220 (2021) 113098

Contents lists available at ScienceDirect

Ultramicroscopy

journal homepage: www.elsevier.com/locate/ultramic

A cartridge-based turning specimen holder with wireless tilt angle measurement for magnetic induction mapping in the transmission electron microscope

Patrick Diehle[*,a,c], András Kovács[*,a], Thomas Duden[a], Rolf Speen[a,1], Kristina Žagar Soderžnik[b], Rafal E. Dunin-Borkowski[a]

[a] Ernst Ruska-Centre for Microscopy and Spectroscopy with Electrons and Peter Grünberg Institute, Forschungszentrum Jülich GmbH, 52425 Jülich, Germany
[b] Jožef Stefan Institute, Department for Nanostructured Materials, Ljubljana, Slovenia
[c] Fraunhofer Institute for Microstructure of Materials and Systems IMWS, Walter-Hülse-Strasse 1, 06120 Halle, Germany

ARTICLE INFO

Keywords:
Transmission electron microscopy
Off-axis electron holography
Magnetic materials
Magnetic induction mapping
Specimen holder
Inclinometer

ABSTRACT

Magnetic induction mapping in the transmission electron microscope using phase contrast techniques such as off-axis electron holography and differential phase contrast imaging often requires the separation of the magnetic contribution to the recorded signal from the electrostatic contribution. When using off-axis electron holography, one of the experimental approaches that can be used to achieve this separation is to evaluate half of the difference between phase shift images that have been recorded before and after turning the sample over. Here, we introduce a cartridge-based sample mounting system, which is based on an existing on-axis tomography specimen holder and can be used to turn a sample over inside the electron microscope, thereby avoiding the need to remove the holder from the microscope to turn the sample over manually. We present three cartridge designs, which are compatible with all pole piece designs and can be used to support conventional 3-mm-diameter sample grids, Si_3N_4-based membrane chips and needle-shaped specimens. We make use of a wireless inclinometer that has a precision of 0.1° to monitor the sample holder tilt angle independently of the microscope goniometer readout. We also highlight the need to remove geometrical image distortions when aligning pairs of phase shift images that have been recorded before and after turning the sample over. The capabilities of the cartridge-based specimen holder and the turning approach are demonstrated by using off-axis electron holography to record magnetic induction maps of lithographically-patterned soft magnetic Co elements, a focused ion beam milled hard magnetic Nd-Fe-B lamella and an array of four Fe_3O_4 nanocrystals.

1. Introduction

Magnetic materials are of interest for applications that range from biomedicine [1–4] to waste water treatment [5], catalysis [6], data storage and nanoelectronic devices [7–14]. The ability to image local variations in the magnetic microstructure of a material with nm spatial resolution and its dependence on parameters such as temperature [15,16], electrical current [17] and applied magnetic field [18] is essential for the fundamental understanding and development of new magnetic materials and devices. The technique of off-axis electron holography can be used to record the phase shift of a high-energy electron wave that has passed through a thin sample in the transmission electron microscope (TEM). The phase shift is, in turn, sensitive to the in-plane component of the magnetic induction within and around the sample [19]. The technique relies on the use of an electron biprism to interfere an electron wave that has passed through the region of interest in the sample with another part of the same electron wave that has passed through vacuum alone (or through a clean region of support film) [20,21]. When examining a magnetic material in the TEM, the conventional microscope objective lens is usually switched off, in order to create a magnetic-field-free environment at the position of the sample [22]. Either an additional non-immersion Lorentz lens or the first transfer lens of an aberration corrector can then be used as the primary imaging lens. Alternatively, magnetic-field-free conditions at the specimen location can be achieved either by using an additional stage between the condenser lens system and the objective lens [23] or by

* Corresponding authors.
E-mail addresses: patrick.diehle@imws.fraunhofer.de (P. Diehle), a.kovacs@fz-juelich.de (A. Kovács).
[1] Deceased May 29, 2020.

https://doi.org/10.1016/j.ultramic.2020.113098
Received 19 January 2020; Received in revised form 26 July 2020; Accepted 26 August 2020
Available online 31 August 2020
0304-3991/ © 2020 The Authors. Published by Elsevier B.V. This is an open access article under the CC BY-NC-ND license (http://creativecommons.org/licenses/BY-NC-ND/4.0/).

using a double objective lens system to cancel the magnetic field at the sample location [24]. The phase shift experienced by the electron wave that has travelled through the sample can be written in the form

$$\varphi(x) = \varphi_{el} + \varphi_{mag} = C_E \int V(x, z)\, dz - \frac{e}{\hbar} \int A_z(x, z)\, dz \quad (1)$$

where φ_{el} and φ_{mag} are the electrostatic and magnetic contributions to the phase shift, respectively, z is the incident electron beam direction, x is a direction perpendicular to z, V is the electrostatic potential, A_z is the component of the magnetic vector potential along z and C_E is a constant that depends on the microscope accelerating voltage [25]. In the absence of long-range charge redistribution in the sample, such as that caused by electron-beam-induced charging, the electrostatic potential is dominated by the mean inner potential (MIP) [26]. Separation of the magnetic and electrostatic contributions to the phase shift is usually achieved by recording electron holographic phase shift images either before and after reversing the magnetisation direction in the sample [27–29] or before and after turning the sample over [30,31], followed by aligning the phase shift images and evaluating half of their difference and half of their sum, respectively. Less commonly, it can also be achieved by recording holograms at two microscope accelerating voltages, or at two sample temperatures (*e.g.*, below and above the Curie temperature of the region of interest) [32].

Reversal of the magnetisation direction in the sample can be performed *in situ* in the TEM either by using a dedicated in-plane magnetising specimen holder [33–36] or by tilting the sample to a chosen angle, switching on the pre-calibrated magnetic field of the conventional microscope objective lens, reducing the field to zero and returning the sample to its initial tilt angle [27,29]. The first option provides access to lower applied magnetic fields than the second one, as a result of the difficulty of manufacturing magnetising coils that are small enough to be used in the restricted space of the microscope pole piece gap. Unfortunately, whichever approach is used, magnetisation reversal may not result in an exactly opposite magnetic state in the sample, leading to artefacts in the final phase difference image and misinterpretation of the experimental results. Magnetisation reversal may also not be suitable for samples that have high magnetic saturation or support complex magnetic states [37].

An approach that involves turning the sample over, retaining its original magnetic state, is therefore favoured. However, it is complicated and time consuming to take the sample out of the microscope, remove it from the specimen holder, turn it over and reinsert it into the specimen holder and the microscope, especially if a precisely defined sample orientation is required. The ability to turn the sample over inside the TEM instead of taking the specimen holder out would avoid needing to handle it. Furthermore, it would avoid exposing the sample to the magnetic return flux of the microscope lenses, which may be significant even when a magnetic-field-free condition has been achieved in the centre of the column, during the sample exchange process. It would also be advantageous for speed and convenience and for retaining the same sample tilt axis, especially when performing multiple tilting or *in situ* experiments on the same sample. The latter capability is important because magnetic phase shift images recorded at different precisely known specimen tilt angles are required to obtain information about the three-dimensional magnetic induction field and magnetisation state of the sample [38–41].

A sample can be turned over inside the TEM by redesigning the stage of the microscope [42] or by using a suitable specimen holder, such as one designed for electron tomography experiments. However, in the past these methods have typically limited the range of samples that could be studied and, in some cases, special sample support geometries were required [43,44]. Here, we describe how an on-axis tomography specimen holder can be modified to allow a wide variety of sample geometries to be turned over inside the TEM, in order to measure their magnetic phase shifts using electron optical phase contrast techniques. The operation of the specimen holder is compatible with all electron microscope pole piece designs. We introduce three cartridges, which can be used to support conventional 3-mm-diameter support grids, Si_3N_4 membrane chips and needle-shaped specimens. The cartridges are optimised to allow a high tilt range and to permit easy handling and flexibility. We equip the specimen holder with an inclinometer, which can be used to measure the holder tilt angle with a precision of 0.1° independently of the microscope goniometer readout and to transfer the measured values wirelessly to a tablet computer.

Although we only present results obtained using the technique of off-axis electron holography, the specimen holder that we describe can equally be used to separate magnetic and electrostatic contributions to signals recorded using other phase contrast techniques, such as differential phase contrast imaging and pixelated scanning TEM, as well as for other experiments that require turning the sample over or precise sample tilting.

2. Materials and methods

The development described below is based on an on-axis Fischione model 2050 tomography specimen holder. Off-axis electron holography experiments were carried out at 300 kV in an FEI (Thermo Fisher Scientific) Titan 60–300 microscope equipped with a high brightness XFEG electron source, an objective lens aberration corrector and a C-TWIN (11 mm gap) pole piece. The objective lens was turned off and the first transfer lens of the aberration corrector was used as a Lorentz lens. The variation in magnetic field at the position of the sample with objective lens current was pre-characterised using a Hall-sensor-equipped TEM specimen holder. In this way, the microscope objective lens current could be adjusted so that the sample was located in magnetic-free conditions or subjected to a chosen vertical magnetic field. The electron optical spatial resolution in Lorentz mode is estimated to be 1.5 ± 0.5 nm. Off-axis electron holograms were recorded on a 2k × 2k Gatan Ultrascan charge-coupled device camera by applying positive voltages in the range of 95 V to 120 V to a biprism positioned close to the conventional selected area aperture plane of the microscope, resulting in holographic interference fringe spacings of approximately 3.1 nm, and 2.8 nm, respectively. An interference width of between 1.6 μm and 1.8 μm was achieved. The acquisition times were between 4 and 8 s and after phase extraction the spatial resolution of the phase information is expected to be between 8.4 nm and 9.3 nm. The recorded off-axis electron holograms were processed using scripts written in the Semper image processing language [45]. Corrections of geometrical distortions in the holograms and analysis of the phase shift images were carried out using scripts written in the Python programming language.

3. Results and discussion

We begin by describing key aspects of the characterisation of the magnetic field experienced by the sample when the microscope is operated in Lorentz mode, not only when the sample is in the centre of the column but also during its exchange. In an FEI (Thermo Fisher Scientific) microscope that is equipped with a regular side entry specimen stage, the sample is inserted into the airlock at a tilt angle of 140°. After pumping, the airlock is opened by manually turning the specimen holder to a tilt angle of 0°. The specimen holder is then inserted to achieve the final sample position in the middle of the column. The two sample orientations are shown schematically in Figs. 1a and 1b.

Fig. 1c shows a Hall probe measurement of the out-of-plane magnetic field that the sample experiences when the specimen holder is inserted into the column of a microscope that is equipped with a C-TWIN pole piece and operated in Lorentz mode at an accelerating voltage of 300 kV. The magnetic field experienced by the sample varies between −6.4 mT and +6 mT as it is inserted into the microscope column, even when the residual magnetic field at the centre of the

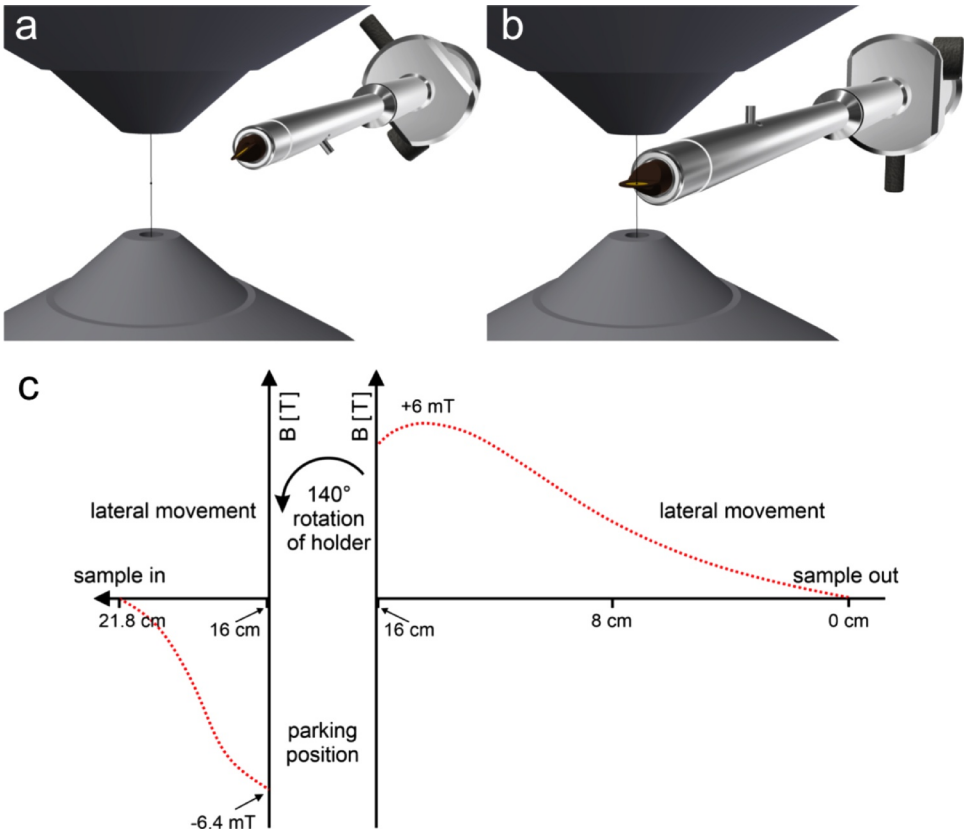

Fig. 1. Schematic diagram showing the sample position during insertion of a specimen holder into an FEI (Thermo Fisher Scientific) Titan microscope: (a) in the parking position and (b) in the final inserted position. (c) Schematic diagram of the variation in out-of-plane magnetic field strength experienced by a sample during insertion into the microscope at 300 kV, based on experimental measurements.

column has been adjusted to below 0.1 mT. As magnetic fields of this magnitude are strong enough to affect the magnetic microstructure of many soft magnetic materials, turning the sample over inside the microscope is the preferred approach to use for separating the magnetic contribution to the recorded signal, even when the microscope is operated in Lorentz mode.

3.1. Cartridges and specimen tilt measurement

The Fischione model 2050 on-axis tomography specimen holder consists of a main body, a cartridge and a needle that holds the sample. The original needle support requires a complicated procedure to mount the sample. In order to achieve compatibility with more commonly used TEM sample geometries, we developed three new cartridges, which can be used to hold conventional 3-mm-diameter TEM support grids, focused ion beam (FIB) milled specimens that are mounted on (*e.g.*, Omniprobe-style) support grids, Si_3N_4 membrane chips and needle-shaped samples. Each cartridge was manufactured from non-magnetic materials, such as copper bronze, copper and titanium. The diameter of each cartridge is 3.75 mm, which allows it to be completely retracted into the specimen holder tube by 6.4 mm and to be turned over irrespective of the objective lens pole piece gap size. Based on the Hall probe measurements described above, the sample in the retracted position is exposed to a magnetic field strength of 0.25 mT. The cartridges, which are labelled 1, 2 and 3 here, are shown in Fig. 2.

Cartridge 1 (Fig. 2a) holds the sample from the top and bottom and provides a tilt range of ± 70°, which is limited by shadowing by the support frame. Cartridge 2 (Fig. 2b) clamps the sample from only one edge and provides an increased tilt range, as there is no additional shadowing by a support frame. Cartridges 1 and 2 are designed to accommodate conventional 3-mm-diameter TEM support grids, FIB-milled specimens mounted on support grids and Si_3N_4 membrane chips. Cartridge 3 (Fig. 2c) offers the possibility of 360° rotation of thin needle-shaped samples, such as those used for atom probe tomography [46,47], which is a complementary method to TEM for three-dimensional structural and chemical characterisation. In cartridges 1 and 2, the sample is fastened by a clamp, which can be moved laterally and is fixed by a screw. In cartridge 3, the needle-shaped sample is fixed by two screws at the top and bottom of the cartridge.

The sample loading procedure involves two steps: i) loading the sample into the cartridge; ii) mounting the cartridge into the on-axis tomography specimen holder. A loading station (Fig. 3) is used to mount TEM samples into the cartridges safely and reliably. First, the cartridge is fixed on the left side of the loading station. For cartridges 1 and 2, loading of the sample follows similar procedures. After retracting the clamp of the cartridge, the sample is placed directly into cartridge 1 or into the loading arm for cartridge 2. A support can be moved below the thin tip of cartridge 1 to prevent mechanical deformation and damage (Fig. 3b). For cartridge 2, the loading station provides precise lateral and vertical adjustment of the loading unit that holds the sample, relative to the clamping mechanism of the cartridge (Fig. 3c). The knob at the lower part of the loading station is used to move a pin in the vertical direction that supports a loading arm used during specimen exchange for cartridge 2. For cartridge 3, the specimen support needle is placed into the cartridge and then fixed by a screw. For mounting each cartridge into the on-axis tomography specimen holder, the original unit (not shown), in which the cartridge is fixed to a retractable mounting arm by a pin going through the hole at the end of the cartridge, is used.

Fig. 4a shows the combined cartridge, tomography specimen holder and inclinometer unit. A magnified view of the sample region shows the attachment of the cartridge to the body of the specimen holder using a pin. During insertion of the specimen holder into the electron microscope, the cartridge is retracted into the specimen holder tube to protect the sample and the thin support frame from inadvertent mechanical damage. Fig. 4b shows the position of the cartridge in the specimen holder during a TEM experiment after moving it out of the tube.

Tilting of the sample is controlled by either the microscope

Fig. 2. Schematic diagrams and photographs of three cartridge designs developed for the on-axis tomography specimen holder. The scale bars on the photographs have lengths of 2 mm. (a) Cartridge 1 holds a conventional 3-mm-diameter TEM support grid and has a tilt range of ± 70°, which is limited by shadowing by the support frame. It can be used for thin or thick samples, including SiN-based membrane chips. (b) Cartridge 2 has a clamping mechanism that provides a full tilt range without shadowing by a support frame. (c) Cartridge 3 is designed to hold needle-shaped samples that have a diameter of 0.25 mm, such as those prepared for characterisation using atom probe tomography.

goniometer or the built-in internal rotation mechanism in the specimen holder. The goniometer is controlled by the microscope control software, which provides an electronic readout of the specimen holder tilt angle. The tilt range of the microscope stage is typically limited to ± 80°. In contrast, the internal tilting mechanism of the on-axis tomography specimen holder is operated manually and allows 360° rotation. The on-axis tomography specimen holder allows the sample to be turned continuously or in fixed steps, in either a clockwise or an anticlockwise direction. A seven-position indexing mechanism offers the possibility to tilt the sample in increments of either 45° or 60°. However, the holder itself does not have an electronic read-out of the sample tilt angle. In order to overcome this limitation, as well as hysteresis and inaccuracy in the operation of the goniometer, an inclinometer unit was attached to the end of the specimen holder to measure its tilt angle independently. Fig. 5 shows a photograph of the specimen holder in the microscope goniometer with the inclinometer unit attached to its end. It consists of a micro-electro-mechanical sensor and a wireless bluetooth transceiver powered by two coin battery cells. A wireless connection to the inclinometer is used to avoid vibrations caused by a cable and to provide an accurate measurement of the tilt position of the holder. Readout of the sample tilt angle is realised using an application programmed in an Android tablet device. As the accuracy of the inclinometer depends on the voltage applied to the sensor and on the temperature of the sensor, these two quantities are recorded together with the specimen holder tilt angle during experiments. Its accuracy also depends on the orientation of the sensor itself. Therefore, a calibration curve was measured, allowing an accuracy of 0.1° to be achieved routinely. The calibration curve was recorded by tilting the

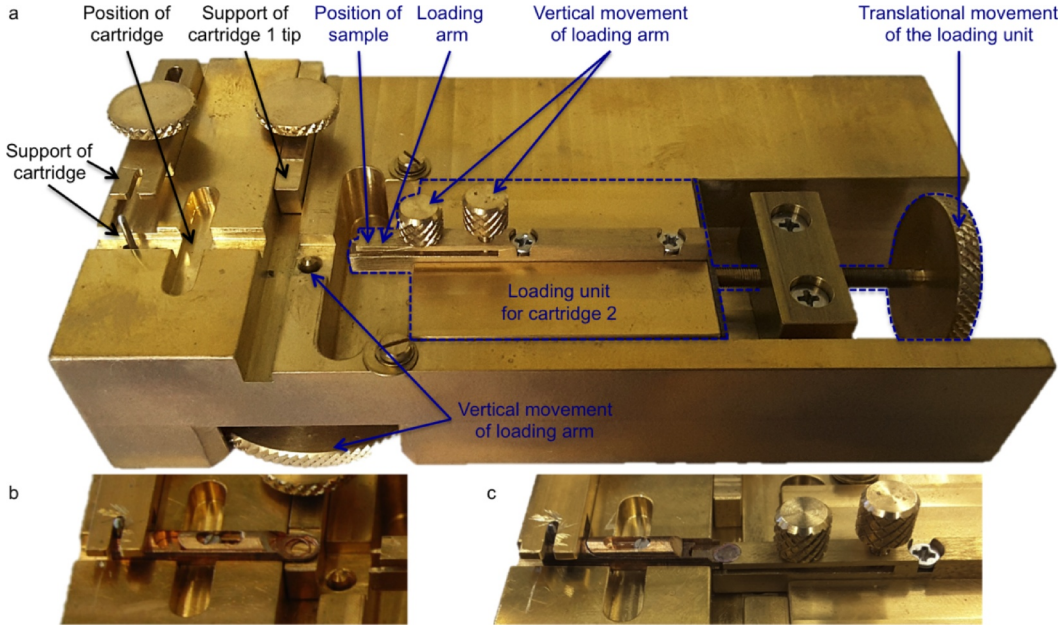

Fig. 3. (a) Photograph of the loading station for mounting a sample into a cartridge. (b) and (c) show cartridges 1 and 2, respectively, inside the loading station during the sample exchange procedure. The cartridge is fastened on the left side of the loading station. A loading unit (marked by a blue dashed line) is used with cartridge 2 to allow precise lateral and vertical adjustment of the sample relative to the clamping mechanism of the cartridge (see image (c)). The length of the loading station is 12 cm. (For interpretation of the references to colour in this figure legend, the reader is referred to the web version of this article.)

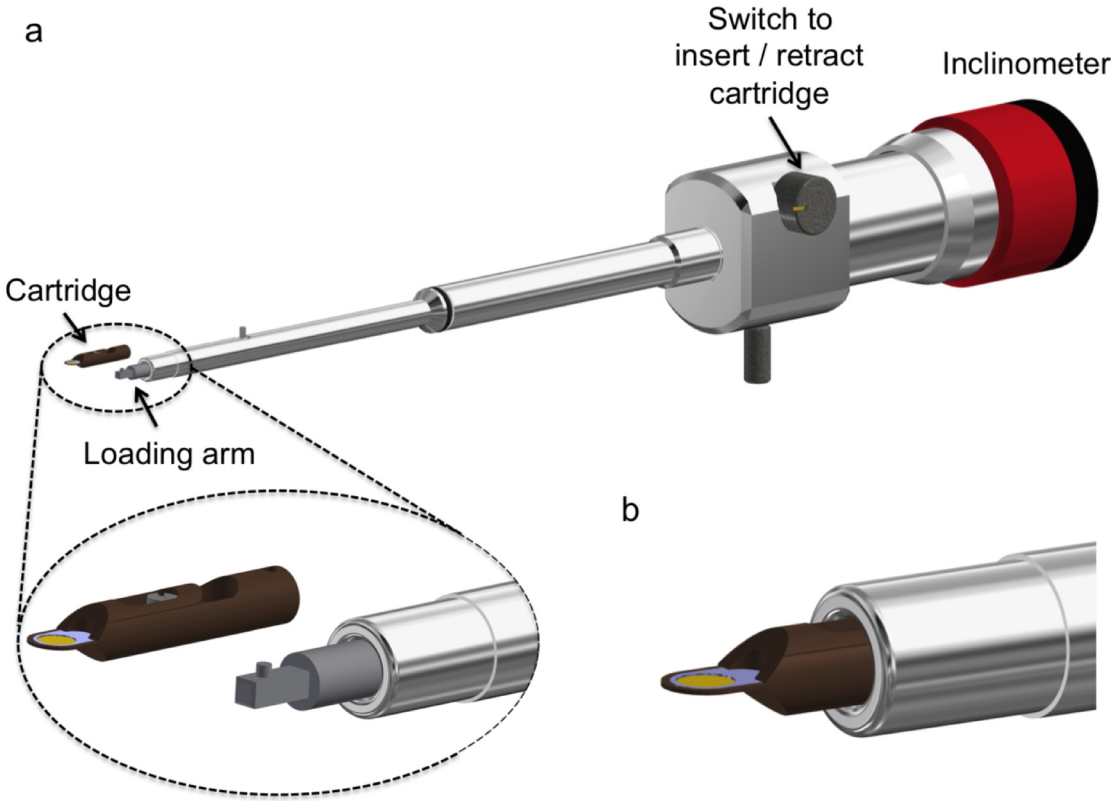

Fig. 4. (a) Schematic diagram showing the cartridge, the on-axis tomography specimen holder and the inclinometer unit. The inset shows a magnified view of the connection between the cartridge and the retractable mounting arm of the holder by a pin. The fully extended position of the mounting arm is only selected during the sample mounting procedure. (b) The position of the cartridge in the specimen holder during a TEM experiment. The position of the cartridge in the specimen holder is controlled by the marked switch. The cartridge is completely retracted into the holder during sample insertion into the microscope goniometer (not shown).

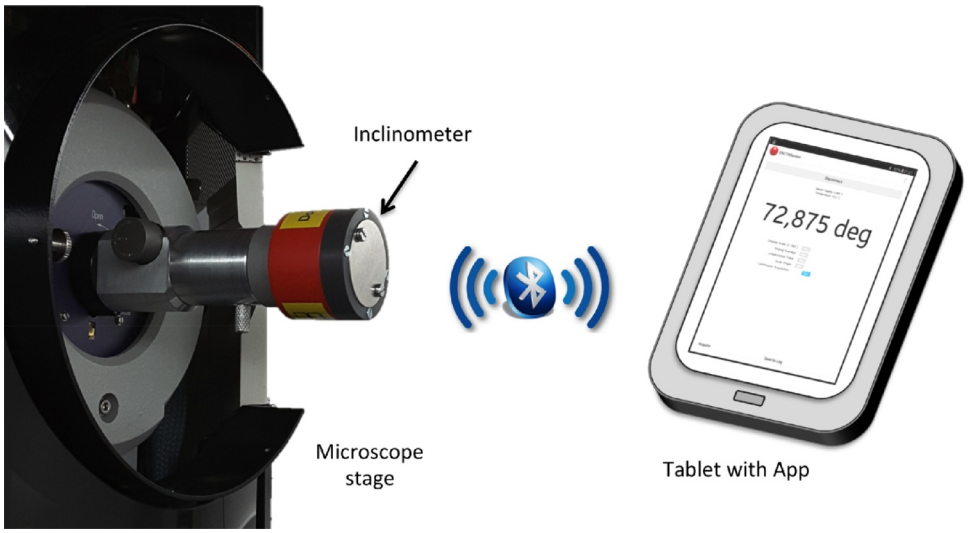

Fig. 5. Photograph of the on-axis tomography specimen holder inserted into the microscope stage, with the inclinometer unit attached to its end, shown alongside a schematic diagram of its wireless connectivity to a tablet computer to record the specimen holder tilt angle.

inclinometer sequentially in 1° steps.

At this point, a clear definition of the tilt angle is required to avoid confusion. Three tilt angles can be distinguished: that of the sample, that of the specimen holder and that of the microscope goniometer. For a conventional single tilt specimen holder, these three angles are normally assumed to be equal. However, as a result of the internal rotation mechanism of the on-axis tomography specimen holder, as well as hysteresis and other mechanical inaccuracies in the goniometer and at the position where the pin of the mounting arm meets the hole at the end of the cartridge (displayed in Fig. 4), the three angles can differ for the present cartridge-based tomography specimen holder. Unless otherwise specified, the tilt angle refers to that of the holder.

For magnetic induction mapping using a technique such as off-axis electron holography, the accuracy and precision of the sample tilt angle are important. An error of $\Delta\theta$ in the angle θ (ideally 180°) by which the sample is turned over can lead to a difference between the projected lengths of regions of the sample in the two recorded images. This difference can introduce artefacts during subtraction to separate the

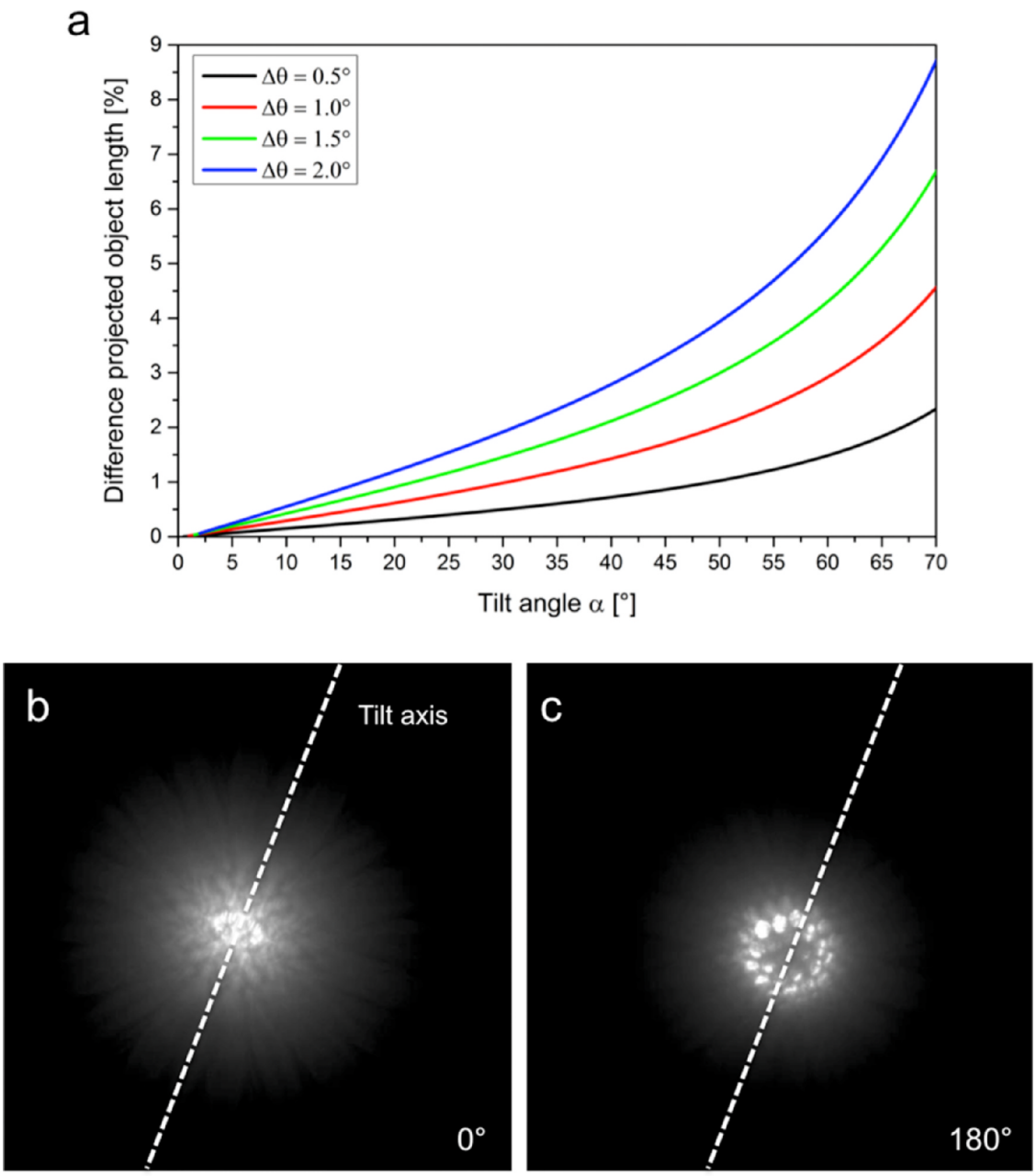

Fig. 6. (a) Influence of an angular turning over error $\Delta\theta$ on the projected length of a feature of interest on the sample plotted as a function of starting sample tilt angle. The percentage difference in projected length between tilt angles of 0° and 180° $\pm$ $\Delta\theta$ is shown for different starting sample tilt angles and different errors $\Delta\theta$ in the turning over angle. (b, c) Representative measurements of turning over error $\Delta\theta$ using CBED patterns recorded from a GaAs single crystalline sample at nominal sample tilt angles of 0° and 180° selected using the seven-position indexing mechanism of the on-axis turning specimen holder. In the present example, a turning over error $\Delta\theta$ of 0.66° is measured. The tilt axis is marked by a dashed white line. (For interpretation of the references to colour in this figure legend, the reader is referred to the web version of this article.)

magnetic from the mean inner potential (MIP) contributions to the signal. Fig. 6a shows the influence of the error $\Delta\theta$ on the difference in projected length of an object plotted as a function of sample tilt angle. An error $\Delta\theta$ of up to 2° can lead to differences of up to 9% in the projected lengths of regions of the sample at higher tilt angles. As stated above, the specimen holder tilt angle (and therefore the turning over angle of the holder) can be controlled to an accuracy of 0.1° with the aid of the inclinometer. However, this does not ensure that the sample itself is turned over with the same accuracy. Therefore, the difference between the specimen holder and sample tilt angles after turning the specimen holder over was measured experimentally. Convergent beam electron diffraction (CBED) patterns of a GaAs single crystal were used to determine the sample tilt angle and hence the error $\Delta\theta$. First, the sample was tilted to the closest crystallographic zone axis of high symmetry using the microscope goniometer, as shown in Fig. 6b. The specimen holder was then turned over manually by 180° using the internal tilting mechanism of the on-axis turning specimen holder and the inclinometer. The holder was rotated only in one direction to minimise backlash. Fig. 6c shows the CBED pattern of the turned over sample. The GaAs crystal is now tilted slightly away from the zone axis orientation. The tilt angle needed to align the crystal again is equivalent to $\Delta\theta$. In practice, the turning over error $\Delta\theta$ was found to be a random error. When using only the seven-position indexing mechanism to turn the sample over, $\Delta\theta$ was measured to be 1.2° on average. When employing the inclinometer, this value was reduced to 0.5° on average. The relatively large value of $\Delta\theta$ in both cases is thought to result from

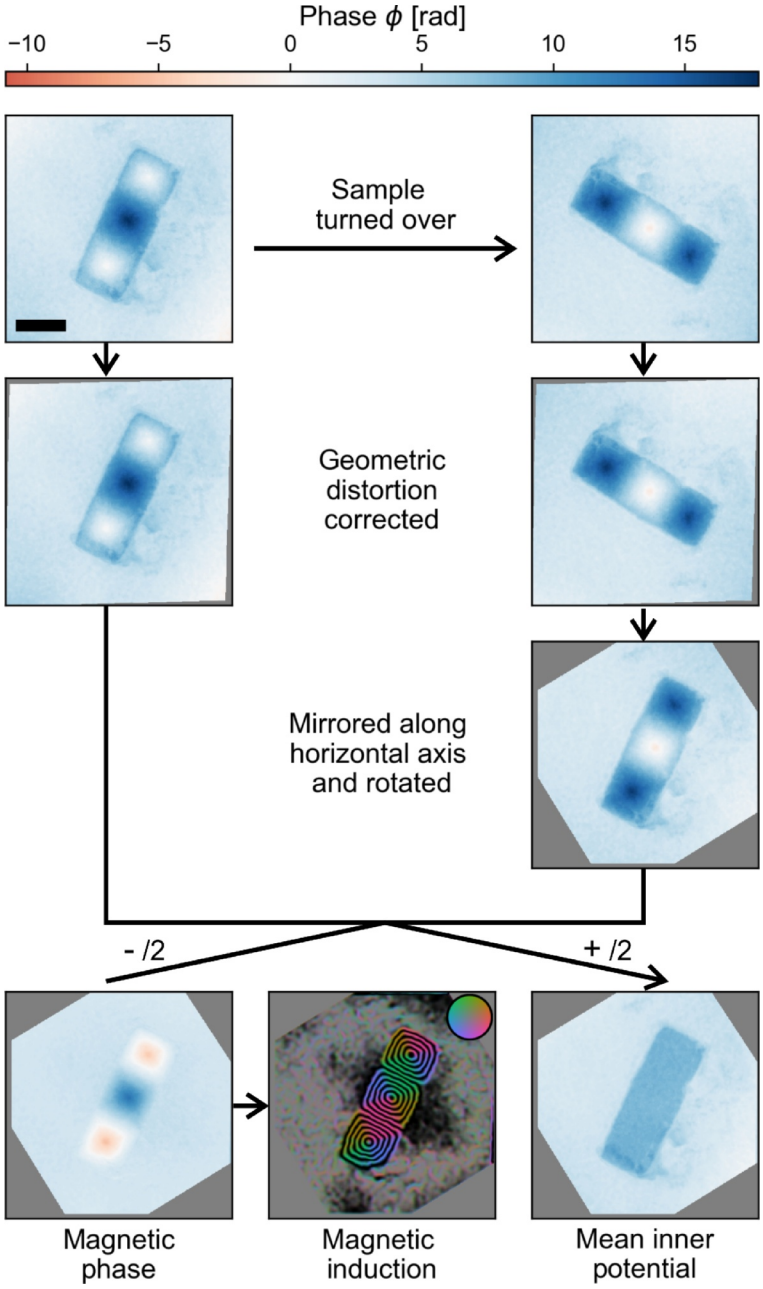

Fig. 7. Processing steps used to generate a magnetic phase shift image by turning the sample over, illustrated for a lithographically patterned 30-nm-thick Co element deposited on a Si_3N_4 membrane. Starting from two reconstructed total phase shift images, geometrical distortions are corrected and the phase shift images are aligned in angle and position. Half of the difference and half of the sum of the two aligned phase shift images are used to obtain the magnetic and MIP contributions to the phase shift, respectively. Magnetic phase contours are then generated by evaluating the *cosine* of a chosen multiple of the magnetic contribution to the phase, while colours are obtained from the gradient of the magnetic contribution to the phase, according to the colour wheel shown. The final magnetic induction map shown in the figure has a contour spacing of $\frac{2\pi}{3}$ rad and reveals the presence of three magnetic vortices. The MIP contribution to the phase shift reveals that a small amount of resist has been left on the Co island and around it after electron beam lithography. Scale bar: 200 nm. (For interpretation of the references to colour in this figure legend, the reader is referred to the web version of this article.)

mechanical instabilities in the internal tilting mechanism of the on-axis turning holder, which are mostly associated with the gearing between the seven-position indexing mechanism and the gap between the mounting arm and the sample cartridge. After turning the sample over, the sample was refocused using the vertical control of the stage (z direction) and fine-tuned by the focus. The height adjustment stayed below 160 μm for the 180° rotated sample relative to the original conditions.

3.2. Magnetic induction mapping by turning the sample over

The advantages of using the turning specimen holder for magnetic induction mapping are now demonstrated through the examination of a rectangular 30-nm-thick Co island that had been deposited onto a 50-nm-thick Si_3N_4 membrane using electron beam lithography. In order to prevent oxidation of the Co film and to reduce electrostatic charging, a 10-nm-thick Al layer was deposited onto its surface. The sample was loaded into the on-axis tomography specimen holder in cartridge 1 (Fig. 2a), initially magnetised out-of-plane using the magnetic field of the objective lens and then examined in magnetic-field-free conditions. Fig. 7 shows an overview of the experimental and digital image processing steps that were used to generate magnetic phase shift images with the turning over method. First, off-axis electron holograms were acquired at 0° and 180° tilt angles selected using the internal tilting mechanism of the on-axis tomography specimen holder and the inclinometer. After 180° rotation, the sample position relative to the biprism was adjusted using the microscope stage movements in order to record close to the same region of interest in the rotated sample and to maintain the same imaging conditions. If the overlap region at the opposite side of the biprism is used, it is also recommended to use the opposite sideband in the reconstruction procedure to get the same sign of the total phase images. At each tilt angle, total phase shift images were reconstructed using object and vacuum reference electron holograms [20]. It was found that the size of the Co element differs between the 0° and 180° sample tilt angles by 4.6% in length and 3.5 % in width. The turning over error can be excluded as an explanation for these

differences, as it would require a turning over error $\Delta\theta$ of approximately 15°. For a typical turning over error $\Delta\theta$ of 0.5°, the expected size difference is negligible for a starting sample tilt angle of 0°. Instead, it was found that the apparent difference in object size results from the presence of geometrical distortions caused by the lens system of the microscope, which is positioned between the sample and the camera [48–52]. The image distortion was measured experimentally and characterised using an Au cross-grating over the magnification range 10k× to 100k×. The Au grid was rotated in-plane by 180° using a dual-axis rotation tomography holder (Fischione model 2040) and an image was recorded every 10°. Changes in distance between characteristic features in the sample during rotation were measured at each magnification. A linear approximation to the distortion field that neglects non-linear terms (e.g. pincushion and barrel contributions) was measured based on the following formula [50]:

$$\begin{pmatrix} x_d \\ y_d \end{pmatrix} = \mathbf{D}\cdot\begin{pmatrix} x \\ y \end{pmatrix}$$
$$\mathbf{D} = \mathbf{R}\begin{pmatrix} d & 0 \\ 0 & 1 \end{pmatrix}\mathbf{R}^{-1} \quad (2)$$

where x_d and y_d are distorted image points, x and y are undistorted image points and **D** is a distortion matrix. The matrix **D** can be decomposed into a rotation matrix **R** by an angle α, a diagonal matrix with a distortion coefficient d as an entry and an inverse rotation matrix $\mathbf{R}^{-1}$ by an angle -α.

A correlation between the distortion coefficient and magnification was observed, which leads to the assumption, that the main contribution to the geometric distortion originates from the projector lens system. However, the contributing effects of the extra lens and the aberration corrector unit are not fully understood yet. Precise measurements of the geometric distortions and correction of non-linear contributions [49,51] will be important factors to improve the image alignment procedure further. The measured linear geometric distortion parameters were used as a starting point to correct the total phase images. In order to contribute for variations of the microscope setup and the associated lenses in the actual experiment, the distortion parameters were adjusted to reduce the difference between both total phase images. For the Co island shown in Fig. 7, a linear distortion correction of 4% at 45° was applied. After correcting for the distortions, the size difference between features in the two phase shift images was below 0.1 %. After distortion correction, the turned-over phase shift image was mirrored, rotated and aligned in angle and position, in order to match the original phase shift image. Half of the difference between the two corrected and aligned phase shift images was used to obtain the magnetic contribution to the phase shift, while half of the sum of the two phase shift images was used to obtain the MIP contribution to the phase shift. The difference images are still observed to contain some small residual misalignment artefacts, which are thought to originate from slight remaining misalignment and non-linear distortions, but they are within a tolerable range. A magnetic induction map was then generated by evaluating the *cosine* of a chosen multiple of the magnetic phase shift, as well as colours from its gradient. The magnetic induction maps reveals the presence of three magnetic vortices inside the Co island. This magnetic state results from magnetising the sample out-of-plane at the beginning of the experiment. It should be noted that the sample could not have been magnetised using the same out-of-plane field in the opposite direction using the objective lens of the microscope, as the available field range is asymmetrical, in the range of −150 mT to +1500 mT. Hence, the turning over approach was the only reliable way to observe the "three-vortex" state in this rectangular Co island in the TEM. Furthermore, a magnetisation reversal experiment can change the magnetic state of such a sample irreproducibly. In order to illustrate this possibility, Fig. 8 compares the magnetising and turning over approaches for an elliptical 30-nm-thick lithographically patterned Co island deposited on a Si_3N_4 membrane. Figs. 8a and 8b show total phase shift images recorded after magnetising the sample in opposite in-plane directions. In this case, the magnetic state did not reverse exactly in the lower part of the ellipse. A magnetic phase shift image calculated in this way would result in a "false" magnetic state. In contrast, Fig. 8c and 8d show total phase shift images obtained by turning the same sample over. The magnetic state is now exactly reversed between the two phase shift images and a final magnetic phase shift image that represents the true magnetic state of the sample can be obtained.

These examples highlight the limitations of using the magnetising approach, in contrast to the turning over approach, for the reliable mapping of magnetic states in nanostructures using electron optical phase contrast techniques such as off-axis electron holography and differential contrast imaging.

3.3. Further applications to hard and soft magnetic materials

Two further examples of the use of the turning specimen holder, when it would be impractical to use other approaches for separating the magnetic and MIP contributions to the phase shift measured using off-axis electron holography, are now presented.

The first example is taken from a study of hard magnetic Tb-doped Nd-Fe-B, which has a saturation magnetic induction of between 1.1 and 1.4 T [53]. A thin TEM sample fabricated from the bulk material usually contains a high density of narrow magnetic domains. The domain wall width is approximately 3.9 nm and scales with magnetic anisotropy [54]. Turning the sample over is the only reliable way to obtain the magnetic phase shift for a hard magnetic material such as Nd-Fe-B, both due to the high magnetic saturation field and due to the rearrangement of the magnetic domain walls after reversing the magnetisation in the sample. In the present experiment, a FIB-milled lamella of Nd-Fe-B was attached to an Omniprobe-style TEM support grid. A turning over off-axis electron holography experiment was carried out inside the TEM using cartridge 1. The procedure described above was used to obtain magnetic phase shift images by turning the sample over. Figs. 9a and 9b show original total phase shift images. A geometrical distortion correction of 4% at 45° was applied to the images before they were aligned and used to obtain the MIP and magnetic contributions to the phase shift (Figs. 9c, d). The final magnetic phase shift image (Fig. 9d) and magnetic induction map (Fig. 9e) show the presence of well-defined 180° magnetic domain walls. However, residual geometrical distortions result in small misalignment artefacts at the edge of the sample in Fig. 9d and 9e. Since the details of the magnetic domain walls were found to be sensitive to the accuracy of the geometrical distortion correction and to the alignment of the phase shift images, their well-defined shapes demonstrate the successful correction of geometrical distortions inside the sample using the present method. Such artefact-free magnetic phase shift images are important for determining magnetic domain wall structures and widths. The local sample thickness can also be determined from the MIP contribution to the phase shift (Fig. 9c).

The second example is taken from a study of an assembly of Fe_3O_4 nanoparticles [55]. As their magnetic coercivity is typically below 50 mT, it is important to avoid exposing the sample to external magnetic fields, as can happen during TEM specimen holder exchange (Fig. 1). Fig. 10 shows experimental results obtained from four Fe_3O_4 crystals with sizes of between 72 and 78 nm in a rectangular arrangement on a holey C film supported on a conventional Cu TEM grid. A turning over experiment was performed using cartridge 1. The sample was initially magnetised by tilting it in the TEM to 70° and applying a 1.4 T magnetic field using the conventional microscope objective lens, before removing the applied field and tilting the sample back to 0°. In off-axis electron holography studies of such crystalline nanoparticles, it is often challenging to find a weakly diffracting condition, such that none of the nanocrystals is close to a Bragg condition. In the present experiment, a weakly diffracting condition was found by tilting the

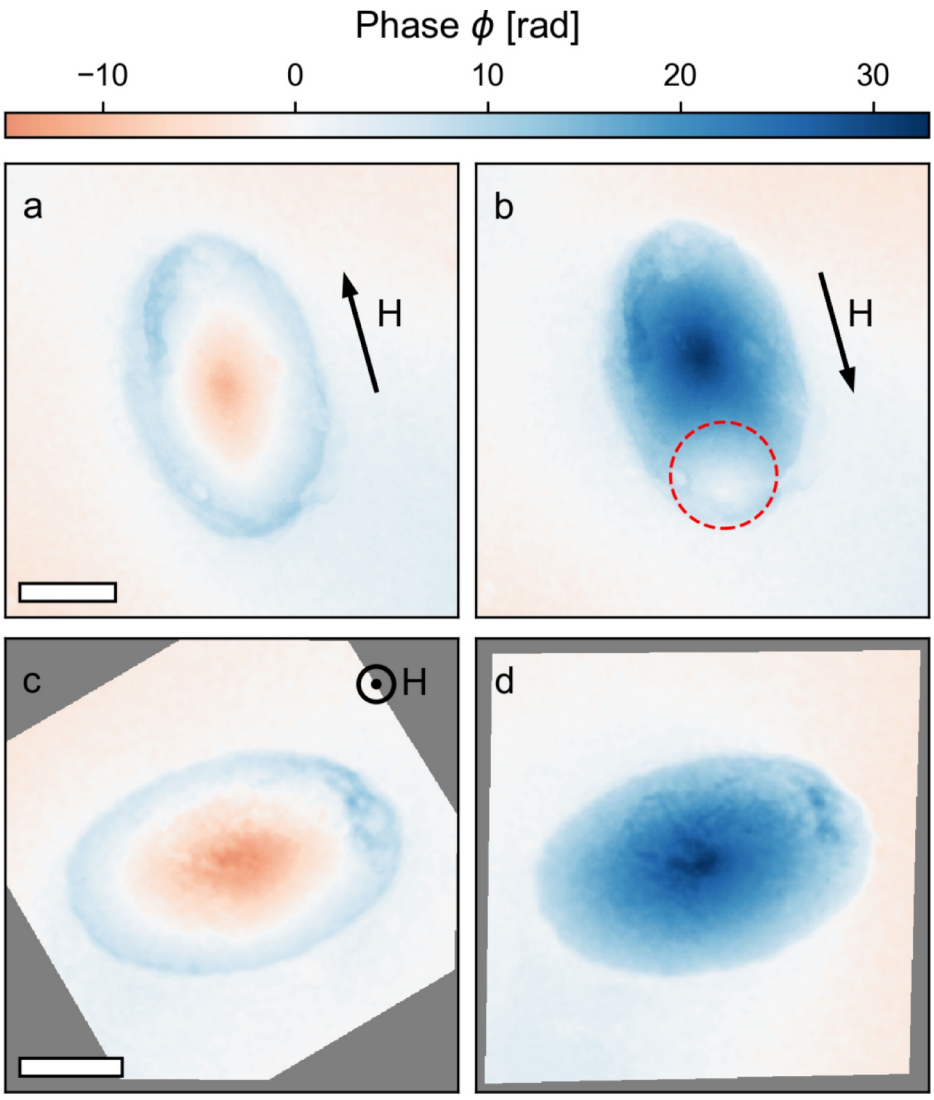

Fig. 8. Comparison between magnetising and turning over approaches to obtain magnetic phase shift images for a lithographically patterned Co ellipse on a SiN membrane. (a, b) Total phase shift images showing two different magnetic states recorded in magnetic-field-free conditions after applying external magnetic fields to the sample with in-plane components in the directions of the black arrows. A dashed red circle highlights an area, where the magnetic state did not reverse exactly. (c, d) Total phase shift images recorded at 0° and 180° tilt angles recorded in magnetic-field-free conditions after initially magnetising the sample out-of-plane. Geometrical distortion correction was applied to (c, d) and (c) was then mirrored and rotated to match (d). Scale bar: 200 nm. (For interpretation of the references to colour in this figure legend, the reader is referred to the web version of this article.)

sample by 8° from its nominally flat orientation. Precise wireless monitoring of the sample tilt angle then allowed it to be turned by 180°. Off-axis electron holograms were recorded before and after turning the sample over inside the microscope. The processing steps described in Fig. 7 were applied, including a geometrical distortion correction of 1 % at 45°. The resulting MIP and magnetic contributions to the phase shift are shown in Fig. 10c and 10d. The presence of slight residual geometrical distortions results in minor misalignment artefacts at the edges of the crystals. The final magnetic induction map shown in Fig. 10e reveals an curling of the magnetisation close to the middle of the nanocrystal assembly [56]. The magnetic phase contours deviate in the upper right crystal in Fig. 10e, perhaps due to the presence of an out-of-plane-magnetised or non-magnetic region. Such a feature could have been misidentified as an artefact if magnetisation reversal had been used to separate the magnetic and MIP contributions to the phase shift.

4. Conclusions and outlook

A cartridge-based modification to an on-axis tomography specimen holder is introduced, in order to allow improved magnetic induction mapping using electron optical phase contrast techniques, including off-axis electron holography and differential phase contrast imaging, by allowing the sample to be turned over inside the TEM. It is then not required to remove the specimen holder from the microscope, which would expose the sample to the magnetic return flux of the microscope lenses. Three different cartridge designs have been developed, in order to accommodate a wide variety of commonly-used TEM sample geometries, including needle-shaped samples. A wireless inclinometer unit has been added to the specimen holder to provide a vibration-free, precise readout of the specimen holder tilt angle on a tablet computer to improve the accuracy and precision of sample tilting. Applications of the turning holder have been presented to studies of lithographically patterned Co islands deposited on a Si_3N_4 membrane chip, a FIB-prepared Nd-Fe-B lamella and an array of four Fe_3O_4 nanoparticles. These examples highlight the wide variety of sample choices and geometries that can be studied using the turning holder. The use of such a turning procedure is highly recommended for samples that have irreproducible magnetic domain structures, high saturation magnetic moments, low coercivities or magnetic states that require out-of-plane magnetic excitation. When compared to other approaches for separating the magnetic contribution to the phase shift recorded using off-axis electron holography, turning the sample over inside the TEM has the advantage that it does not change the magnetic state of the sample, as well as offering flexibility for magnetic vector field tomography [38,44,57]. Although our design is limited to a single tilt axis, in contrast to other designs that enable the recording of two orthogonal tilt series in a single experiment [44], it has the advantage of being able to accommodate many sample geometries. Future developments of the cartridge and holder design may introduce possibilities to apply electrical bias

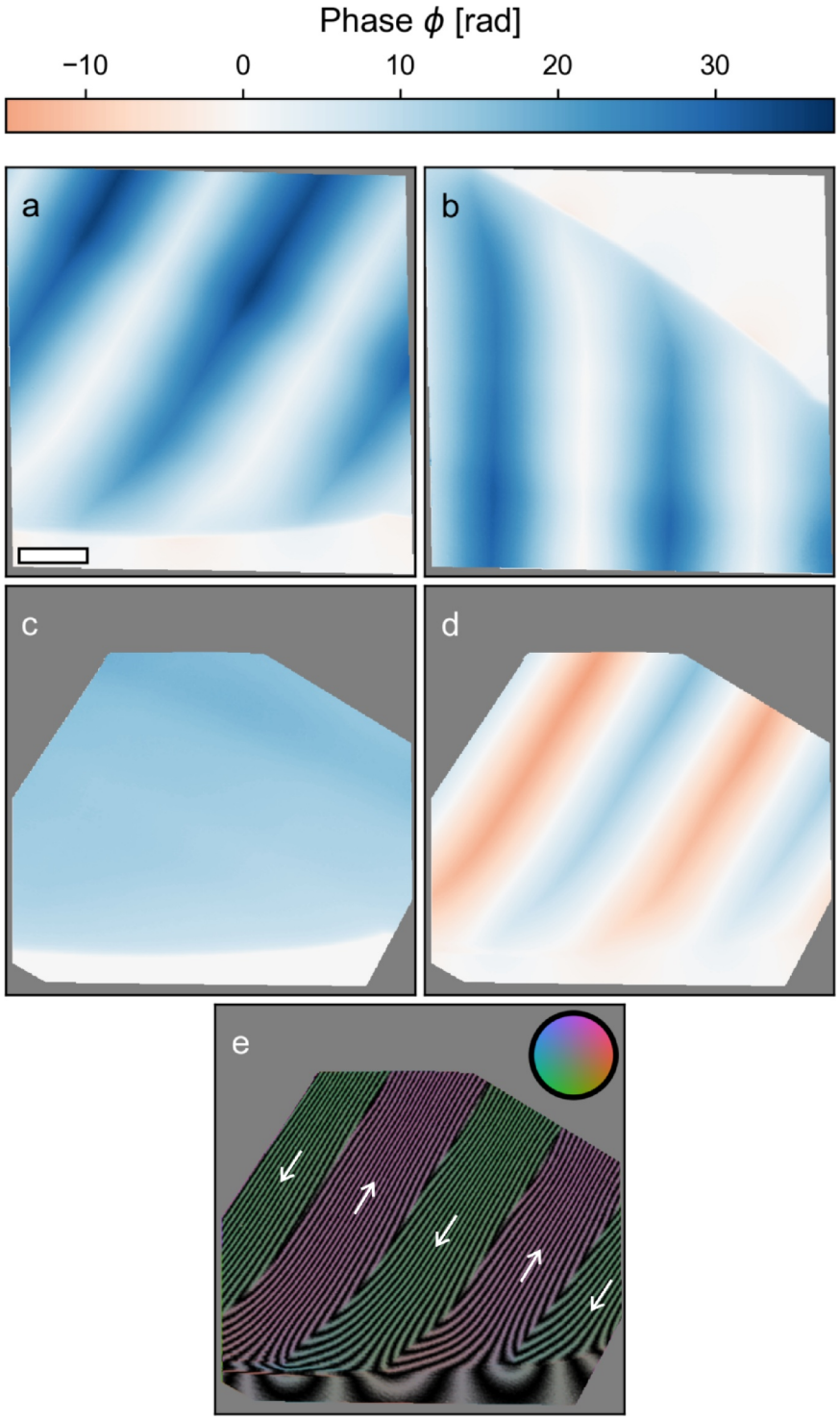

Fig. 9. Magnetic domain structure of a FIB-prepared Tb-doped Nd-Fe-B sample. (a, b) Total phase shift images recorded at sample tilt angles of 0° and 180°. (c, d) MIP and magnetic contributions to the phase shift, respectively, determined after removing geometrical distortions and aligning the resulting phase shift images in angle and position. (e) Final magnetic induction map. White arrows show the directions of the magnetic domains. The phase contour spacing is $\frac{\pi}{2}$ rad. Scale bar: 200 nm. (For interpretation of the references to colour in this figure legend, the reader is referred to the web version of this article.)

potentials to the sample and to control the temperature of the sample either using heating or cooling. These add-ons are technically not impossible to implement, but represent major challenges to electro-mechanical engineering of the manufacturing process of the cartridge and TEM tube elements.

Declaration of Competing Interest

The authors declare that they have no known competing financial interests or personal relationships that could have appeared to influence the work reported in this paper.

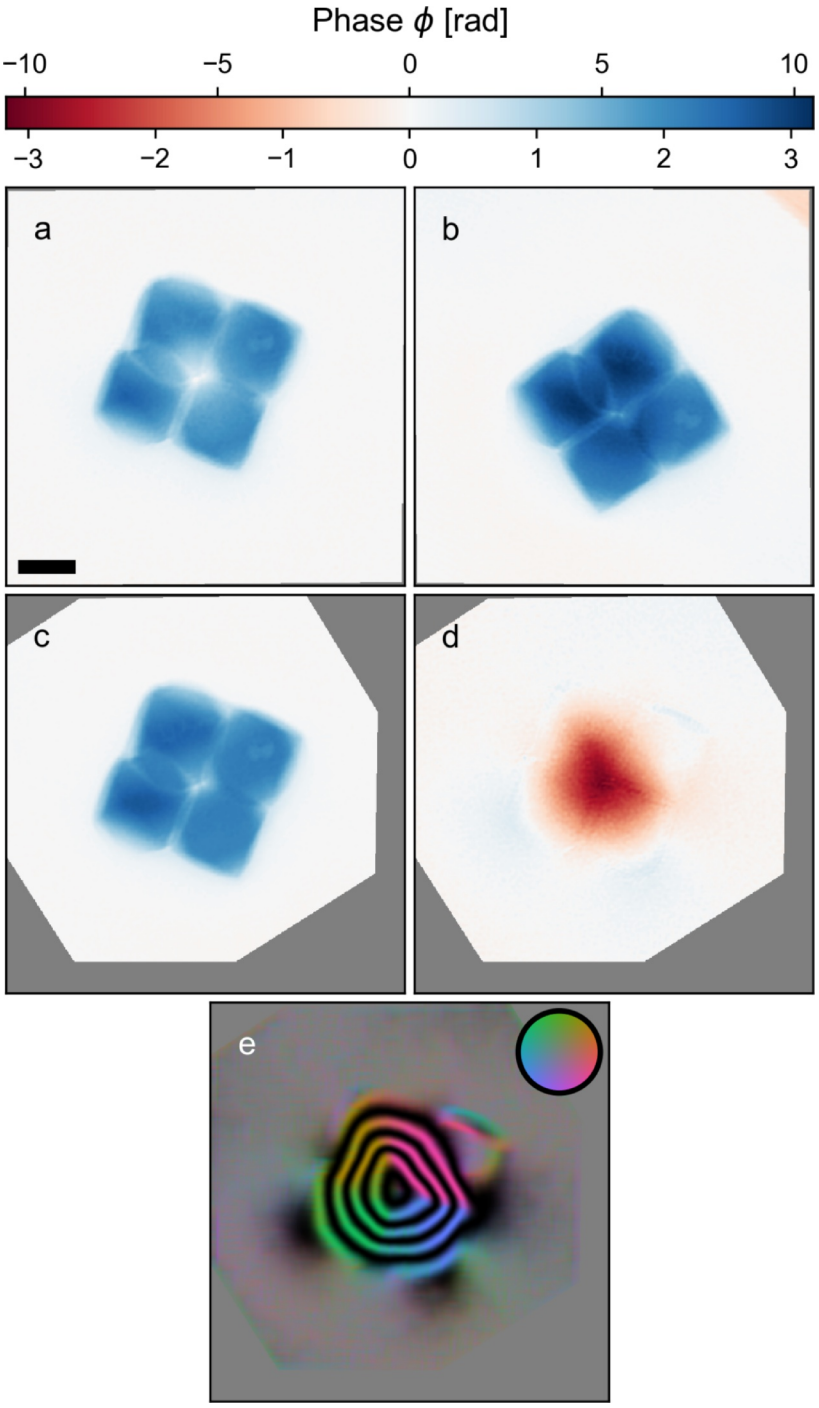

Fig. 10. Magnetic induction mapping of four magnetite (Fe_3O_4) nanocrystals. (a, b) Total phase shift images recorded at sample tilt angles of 8° and 188°, respectively. (c, d) MIP and magnetic contributions to the phase shift, respectively. The upper scale of the colour bar refers to (a–c), while the lower scale refers to (d). (e) Magnetic induction map obtained by generating contours of spacing $\frac{\pi}{4}$ rad and colours from the magnetic contribution to the phase shift. Scale bar: 50 nm. (For interpretation of the references to colour in this figure legend, the reader is referred to the web version of this article.)

Acknowledgments

The authors would like to thank Zi-An Li and Alexandra Terrey for providing samples, Juri Barthel for contributions to the geometric image distortion correction, Max Kruth and Werner Pieper for technical support and Alan Robins for valuable comments. Contribution: PD, REDB and AK conceived project and designed the experiments, PD performed the experiments and carried out the analysis, TD designed the inclinometer, PD and RS designed the cartridges. The manuscript was prepared by PD, AK and REDB, with contributions from KZS. All authors discussed the results and commented on the manuscript. Funding: This project has received funding from the European Research Council (ERC) under the European Union's 7th Framework programme grant agreement No. 320832, Horizon 2020 Research and Innovation Programme under grant agreement No.856538 and under grant agreement No.823717-ESTEEM3. This project was supported by the Deutsche Forschungsgemeinschaft (DFG, German Research Foundation) through Project-ID 405553726 – TRR 270 and by the DARPA TEE program through grant MIPR# HR0011831554.

References

[1] P. Tartaj, M. del Puerto Morales, S. Veintemillas-Verdaguer, T. González-Carreño, C.J. Serna, The preparation of magnetic nanoparticles for applications in biomedicine, J. Phys. D: Appl. Phys. 36 (13) (2003) R182.

[2] Q.A. Pankhurst, J. Connolly, S.K. Jones, J. Dobson, Applications of magnetic nanoparticles in biomedicine, J. Phys. D: Appl. Phys. 36 (13) (2003) R167.

[3] W. Wu, Z. Wu, T. Yu, C. Jiang, W.-S. Kim, Recent progress on magnetic iron oxide nanoparticles: synthesis, surface functional strategies and biomedical applications, Sci. Technol. Adv. Mater. 16 (2) (2015) 23501, https://doi.org/10.1088/1468-6996/16/2/023501.

[4] N.A. Frey, S. Peng, K. Cheng, S. Sun, Magnetic nanoparticles: synthesis, functionalization, and applications in bioimaging and magnetic energy storage, Chem. Soc. Rev. 38 (2009) 2532–2542, https://doi.org/10.1039/B815548H.

[5] P. Xu, G.M. Zeng, D.L. Huang, C.L. Feng, S. Hu, M.H. Zhao, C. Lai, Z. Wei, C. Huang, G.X. Xie, Z.F. Liu, Use of iron oxide nanomaterials in wastewater treatment: a review, Sci. Total Environ. 424 (2012) 1–10, https://doi.org/10.1016/j.scitotenv.2012.02.023.

[6] J. Govan, Y.K. Gun'ko, Recent advances in the application of magnetic nanoparticles as a support for homogeneous catalysts, Nanomaterials 4 (2) (2014) 222–241, https://doi.org/10.3390/nano4020222.

[7] S. Sun, C.B. Murray, D. Weller, L. Folks, A. Moser, Monodisperse FePt nanoparticles and ferromagnetic FePt nanocrystal superlattices, Science 287 (5460) (2000) 1989–1992, https://doi.org/10.1126/science.287.5460.1989.

[8] A. Moser, K. Takano, D.T. Margulies, M. Albrecht, Y. Sonobe, Y. Ikeda, S. Sun, E.E. Fullerton, Magnetic recording: advancing into the future, J. Phys. D: Appl. Phys. 35 (19) (2002) R157.

[9] B.D. Terris, T. Thomson, Nanofabricated and self-assembled magnetic structures as data storage media, J. Phys. D: Appl. Phys. 38 (12) (2005) R199.

[10] S. Singamaneni, V.N. Bliznyuk, C. Binek, E.Y. Tsymbal, Magnetic nanoparticles: recent advances in synthesis, self-assembly and applications, J. Mater. Chem. 21 (2011) 16819–16845, https://doi.org/10.1039/C1JM11845E.

[11] M.H. Kryder, E.C. Gage, T.W. McDaniel, W.A. Challener, R.E. Rottmayer, G. Ju, Y.T. Hsia, M.F. Erden, Heat assisted magnetic recording, Proc. IEEE 96 (11) (2008) 1810–1835, https://doi.org/10.1109/JPROC.2008.2004315.

[12] R.L. Stamps, S. Breitkreutz, J. Åkerman, A.V. Chumak, Y. Otani, G.E.W. Bauer, J.-U. Thiele, M. Bowen, S.A. Majetich, M. Kläui, I.L. Prejbeanu, B. Dieny, N.M. Dempsey, B. Hillebrands, The 2014 magnetism roadmap, J. Phys. D: Appl. Phys. 47 (33) (2014) 333001.

[13] B.C. Stipe, T.C. Strand, C.C. Poon, H. Balamane, T.D. Boone, J.A. Katine, J.-L. Li, V. Rawat, H. Nemoto, A. Hirotsune, O. Hellwig, R. Ruiz, E. Dobisz, D.S. Kercher, N. Robertson, T.R. Albrecht, B.D. Terris, Magnetic recording at 1.5 Pb m^{-2}using an integrated plasmonic antenna, Nat. Photon. 4 (7) (2010) 484–488.

[14] A.A. Ünal, S. Valencia, F. Radu, D. Marchenko, K.J. Merazzo, M. Vázquez, J. Sánchez-Barriga, Ferrimagnetic $DyCo_5$ nanostructures for bits in heat-assisted magnetic recording, Phys. Rev. Appl. 5 (2016) 064007, https://doi.org/10.1103/PhysRevApplied.5.064007.

[15] C. Gatel, B. Warot-Fonrose, N. Biziere, L. Rodríguez González, D. Reyes, R. Cours, M. Castiella, M.J. Casanove, Inhomogeneous spatial distribution of the magnetic transition in an iron-rhodium thin film, Nat. Commun. 8 (2017) 15703, https://doi.org/10.1038/ncomms15703.

[16] T.P. Almeida, A.R. Muxworthy, A. Kovács, W. Williams, P.D. Brown, R.E. Dunin-Borkowski, Direct visualization of the thermomagnetic behavior of pseudo–single-domain magnetite particles, Sci. Adv. 2 (4) (2016), https://doi.org/10.1126/sciadv.1501801.

[17] X.Z. Yu, D. Morikawa, Y. Tokunaga, M. Kubota, T. Kurumaji, H. Oike, M. Nakamura, F. Kagawa, Y. Taguchi, T. Arima, M. Kawasaki, Y. Tokura, Current-induced nucleation and annihilation of magnetic skyrmions at room temperature in a chiral magnet, Adv. Mater. 29 (21) (2017) 1606178, https://doi.org/10.1002/adma.201606178.

[18] C. Jin, Z. Li, A. Kovács, J. Caron, F. Zheng, F. Rybakov, N. Kiselev, H. Du, S. Blügel, M. Tian, Y. Zhang, M. Farle, R. Dunin-Borkowski, Control of morphology and formation of highly geometrically confined magnetic skyrmions, Nat. Commun. 8 (2017) 15569, https://doi.org/10.1038/ncomms15569.

[19] R.E. Dunin-Borkowski, T. Kasama, M.R. McCartney, D.J. Smith, Electron holography, in: P.W. Hawkes, J.C.H. Spence (Eds.), Science of Microscopy, Springer, 2006, pp. 1141–1195.

[20] M.R. McCartney, D.J. Smith, Electron holography: phase imaging with nanometer resolution, Annu. Rev. Mater. Res. 37 (2007) 729–767, https://doi.org/10.1146/annurev.matsci.37.052506.084219.

[21] P.A. Midgley, R.E. Dunin-Borkowski, Electron tomography and holography in materials science, Nat. Mater. 8 (2009) 271–280, https://doi.org/10.1038/nmat2406.

[22] T. Kasama, R. Dunin-Borkowski, M. Beleggia, Electron holography of magnetic materials, in: F.A.M. Ramirez (Ed.), Holography, IntechOpen, Rijeka, 2011.

[23] E. Snoeck, F. Houdellier, Y. Taniguchi, A. Masseboeuf, C. Gatel, J. Nicolai, M. Hÿtch, Off-axial aberration correction using a B-COR for Lorentz and HREM modes, Microsc. Microanal. 20 (S3) (2014) 932–933, https://doi.org/10.1017/S1431927614006382.

[24] N. Shibata, Y. Kohno, A. Nakamura, S. Morishita, T. Seki, A. Kumamoto, H. Sawada, T. Matsumoto, S.D. Findlay, Y. Ikuhara, Atomic resolution electron microscopy in a magnetic field free environment, Nat. Commun. 10 (2019) 2308, https://doi.org/10.1038/s41467-019-10281-2.

[25] H. Kohl, L. Reimer, Transmission Electron Microscopy: Physics of Image Formation., Springer Series in Optical Sciences; vol. 36, 2008.

[26] J. Spence, On the accurate measurement of structure–factor amplitudes and phases by electron diffraction, Acta Crystallograph. Sect. A 49 (2) (1993) 231–260, https://doi.org/10.1107/S0108767392005087.

[27] R.E. Dunin-Borkowski, M.R. McCartney, D.J. Smith, S.S.P. Parkin, Towards quantitative electron holography of magnetic thin films using in situ magnetization reversal, Ultramicroscopy 74 (1–2) (1998) 61–73, https://doi.org/10.1016/S0304-3991(98)00023-0.

[28] T. Kasama, R.E. Dunin-Borkowski, M.R. Scheinfein, S.L. Tripp, J. Liu, A. Wei, Reversal of flux closure states in cobalt nanoparticle rings with coaxial magnetic pulses, Adv. Mater. 20 (22) (2008) 4248–4252, https://doi.org/10.1002/adma.200702941.

[29] L.A. Rodríguez, C. Magén, E. Snoeck, C. Gatel, L. Marín, L. Serrano-Ramón, J.L. Prieto, M. Muñoz, P.A. Algarabel, L. Morellon, J.M.D. Teresa, M.R. Ibarra, Quantitative in situ magnetization reversal studies in lorentz microscopy and electron holography, Ultramicroscopy 134 (2013) 144–154, https://doi.org/10.1016/j.ultramic.2013.06.003.

[30] N. Biziere, C. Gatel, R. Lassalle-Balier, M.C. Clochard, J.E. Wegrowe, E. Snoeck, Imaging the fine structure of a magnetic domain wall in a Ni nanocylinder, Nano Lett. 13 (5) (2013) 2053–2057, https://doi.org/10.1021/nl400317j.

[31] A. Tonomura, T. Matsuda, J. Endo, T. Arii, K. Mihama, Holographic interference electron microscopy for determining specimen magnetic structure and thickness distribution, Phys. Rev. B 34 (1986) 3397–3402.

[32] A. Kovács, Z. Li, K. Shibata, R.E. Dunin-Borkowski, Lorentz microscopy and off-axis electron holography of magnetic skyrmions in FeGe, Resolut. Discov. 1 (1) (2016) 2–8, https://doi.org/10.1556/2051.2016.00037.

[33] A. Budruk, C. Phatak, A.K. Petford-Long, M.D. Graef, In situ lorentz TEM magnetization studies on a Fe-Pd-Co martensitic alloy, Acta Mater. 59 (17) (2011) 6646–6657, https://doi.org/10.1016/j.actamat.2011.07.020.

[34] G. Yi, W.A.P. Nicholson, C.K. Lim, J.N. Chapman, S. McVitie, C.D.W. Wilkinson, A new design of specimen stage for in situ magnetising experiments in the transmission electron microscope, Ultramicroscopy 99 (1) (2004) 65–72, https://doi.org/10.1016/S0304-3991(03)00148-7.

[35] T. Uhlig, M. Heumann, J. Zweck, Development of a specimen holder for in situ generation of pure in-plane magnetic fields in a transmission electron microscope, Ultramicroscopy 94 (3) (2003) 193–196, https://doi.org/10.1016/S0304-3991(02)00264-4.

[36] M. Arita, R. Tokuda, K. Hamada, Y. Takahashi, Development of TEM holder generating in-plane magnetic field used for in-situ TEM observation, Mater. Trans. 55 (3) (2014) 403–409, https://doi.org/10.2320/matertrans.MD201310.

[37] J. Llandro, D.M. Love, A. Kovács, J. Caron, K.N. Vyas, A. Kákay, R. Salikhov, K. Lenz, J. Fassbender, M.R.J. Scherer, C. Cimorra, U. Steiner, C.H.W. Barnes, R.E. Dunin-Borkowski, S. Fukami, H. Ohno, Visualizing magnetic structure in 3d nanoscale Ni-Fe gyroid networks, Nano Lett. 20 (5) (2020) 3642–3650, https://doi.org/10.1021/acs.nanolett.0c00578.

[38] D. Wolf, L.A. Rodriguez, A. Béché, E. Javon, L. Serrano, C. Magen, C. Gatel, A. Lubk, H. Lichte, S. Bals, G.V. Tendeloo, A. Fernández-Pacheco, J.M.D. Teresa, E. Snoeck, 3D Magnetic induction maps of nanoscale materials revealed by electron holographic tomography, Chem. Mater. 27 (19) (2015) 6771–6778, https://doi.org/10.1021/acs.chemmater.5b02723.

[39] T. Tanigaki, Y. Takahashi, T. Shimakura, T. Akashi, R. Tsuneta, A. Sugawara, D. Shindo, Three-dimensional observation of magnetic vortex cores in stacked ferromagnetic discs, Nano Lett. 15 (2) (2015) 1309–1314, https://doi.org/10.1021/nl504473a.

[40] G. Lai, T. Hirayama, A. Fukuhara, K. Ishizuka, T. Tanji, A. Tonomura, Three-dimensional reconstruction of magnetic vector fields using electron-holographic interferometry, J. Appl. Phys. 75 (9) (1994) 4593–4598, https://doi.org/10.1063/1.355955.

[41] S.J. Lade, D. Paganin, M.J. Morgan, Electron tomography of electromagnetic fields, potentials and sources, Opt. Commun. 253 (4–6) (2005) 392–400, https://doi.org/10.1016/j.optcom.2005.04.071.

[42] C.V. Iancu, E.R. Wright, J. Benjamin, W.F. Tivol, D.P. Dias, G.E. Murphy, R.C. Morrison, J.B. Heymann, G.J. Jensen, A "flip–flop" rotation stage for routine dual-axis electron cryotomography, J. Struct. Biol. 151 (3) (2005) 288–297, https://doi.org/10.1016/j.jsb.2005.07.004.

[43] K. Jarausch, D.N. Leonard, Three-dimensional electron microscopy of individual nanoparticles, J. Electron. Microsc. 58 (3) (2009) 175–183, https://doi.org/10.1093/jmicro/dfn028.

[44] R. Tsuneta, H. Kashima, T. Iwane, K. Harada, M. Koguchi, Dual-axis 360° rotation specimen holder for analysis of three-dimensional magnetic structures, Microscopy 63 (6) (2014) 469–473, https://doi.org/10.1093/jmicro/dfu030.

[45] W.O. Saxton, T.J. Pitt, M. Horner, Digital image processing: the Semper system, Ultramicroscopy 4 (3) (1979) 343–353, https://doi.org/10.1016/S0304-3991(79)80044-3.

[46] D. Raabe, S. Ohsaki, K. Hono, Mechanical alloying and amorphization in Cu-Nb-Ag in situ composite wires studied by transmission electron microscopy and atom probe tomography, Acta Mater. 57 (17) (2009) 5254–5263, https://doi.org/10.1016/j.actamat.2009.07.028.

[47] Y. Toji, H. Matsuda, M. Herbig, P.-P. Choi, D. Raabe, Atomic-scale analysis of carbon partitioning between martensite and austenite by atom probe tomography and correlative transmission electron microscopy, Acta Mater. 65 (2014) 215–228, https://doi.org/10.1016/j.actamat.2013.10.064.

[48] P.W. Hawkes, E. Kasper, Chapter 24 - the geometrical aberrations of round lenses, in: P. Hawkes, E. Kasper (Eds.), Principles of Electron Optics, Academic Press, San Diego, 1996, pp. 339–392.

[49] F. Hue, C.L. Johnson, S. Lartigue-Korinek, G. Wang, P.R. Buseck, M.J. Hÿtch, Calibration of projector lens distortions for quantitative high-resolution TEM, Microsc. Microanal. 11 (2005) 552–553, https://doi.org/10.1017/

S143192760551081X.
[50] H. Lichte, D. Geiger, A. Harscher, E. Heindl, M. Lehmann, D. Malamidis, A. Orchowski, W.-D. Rau, Artefacts in electron holography, Ultramicroscopy 64 (1?4) (1996) 67–77, https://doi.org/10.1016/0304-3991(96)00018-6.
[51] V. Kaynig, B. Fischer, E. Müller, J.M. Buhmann, Fully automatic stitching and distortion correction of transmission electron microscope images, J. Struct. Biol. 171 (2) (2010) 163–173, https://doi.org/10.1016/j.jsb.2010.04.012.
[52] G.C. Capitani, P. Oleynikov, S. Hovmöller, M. Mellini, A practical method to detect and correct for lens distortion in the TEM, Ultramicroscopy 106 (2) (2006) 66–74, https://doi.org/10.1016/j.ultramic.2005.06.003.
[53] M. Soderžnik, M. Korent, K. Žagar Soderžnik, M. Katter, K. Üstüner, S. Kobe, High-coercivity Nd-Fe-B magnets obtained with the electrophoretic deposition of sub-micron TbF_3 followed by the grain-boundary diffusion process, Acta Mater. 115 (2016) 278–284, https://doi.org/10.1016/j.actamat.2016.06.003.
[54] J.M.D. Coey, Magnetism and Magnetic Materials, Cambridge University Press, Cambridge, 2010.
[55] D. Kim, N. Lee, M. Park, B.H. Kim, K. An, T. Hyeon, Synthesis of uniform ferrimagnetic magnetite nanocubes, J. Am. Chem. Soc. 131 (2) (2009) 454–455, https://doi.org/10.1021/ja8086906.
[56] E. Snoeck, C. Gatel, L.M. Lacroix, T. Blon, S. Lachaize, J. Carrey, M. Respaud, B. Chaudret, Magnetic configurations of 30 nm iron nanocubes studied by electron holography, Nano Lett. 8 (12) (2008) 4293–4298, https://doi.org/10.1021/nl801998x.
[57] D. Wolf, A. Lubk, F. Röder, H. Lichte, Electron holographic tomography, Curr. Opin. Solid State Mater. Sci. 17 (3) (2013) 126–134, https://doi.org/10.1016/j.cossms.2013.05.002.